Bulletin of the Seismological Society of America, Vol. 109, No. 5, pp. 2009–2020, October 2019, doi: 10.1785/0120190061

Dynamic Rupture Simulations of the 1920 M_S 8.5 Haiyuan Earthquake in China

by Xiurong Xu, Zhenguo Zhang, Feng Hu, and Xiaofei Chen

Abstract The Haiyuan fault is a major seismogenic fault on the northeastern edge of the Tibetan–Qinghai plateau. The 16 December 1920 M_S 8.5 Haiyuan, China, earthquake is the largest and most recent event along the eastern Haiyuan fault (the Haiyuan fault in the article). Because only a few near-field seismic recordings are available, the rupture process remains unclear. To understand the source process and intensity distribution of the 1920 Haiyuan earthquake, we simulated the dynamic rupture and strong ground motion of said earthquake using the 3D curved-grid finite-difference method. Considering the differences in epicenter locations among various catalogs, we constructed two models with different source points. For each model, three versions with different fault geometries were investigated: one continuous fault model and two discontinuous fault models with different stepover widths (1.8 and 2.5 km, respectively). A dynamic rupture source model with a final slip distribution similar to that observed on the ground surface was found. The maximum displacement on the ground surface was ~6.5 m. Based on the dynamic rupture model, we also simulated the strong ground motion and estimated the theoretical intensity distribution. The maximum value of the horizontal peak ground velocity occurs near Haiyuan County, where the intensity reaches XI. Without considering the site conditions, the intensity values in most regions, based on the dynamic scenarios, are smaller than the values from field investigation. In this work, we present physically based insights into the 1920 Haiyuan earthquake, which is important for understanding rupture processes and preventing seismic hazards on the northeastern boundary of the Tibetan plateau.

Introduction

The 16 December 1920 M_S 8.5 Haiyuan, China, earthquake was one of the largest, most devastating intraplate earthquakes across the world during the early twentieth century. This earthquake caused nearly 270,000 deaths, the destruction of thousands of villages, and serious secondary disasters (Lanzhou Institute of Seismology and the Seismological Bureau of Ningxia-Hui Autonomous Region, 1980). In addition, the 1920 Haiyuan earthquake with a maximum intensity value of XII had a nearly 237 km surface rupture length and 10–11 m maximum sinistral strike-slip dislocation (Institute of Geology, China Earthquake Administration and the Seismological Bureau of Ningxia-Hui Autonomous Region, 1990). Six aftershocks with magnitudes over 5 were recorded within three years after the 1920 Haiyuan earthquake (Fig. 1a). Among them, an aftershock with a magnitude of ~7 occurred east of the mainshock. The seismogenic fault (the Haiyuan fault) is located on the northeastern margin of the Tibetan plateau, at the junction of the Alxa block, the Ordos block, and the Qinghai–Tibet block (Fig. 1b). It primarily extends along the sides of strongly uplifted mountains and has a linear trend (Shi *et al.*, 2013). There have been 17 paleoearthquake events on the seismogenic fault through studies on trenches, one of which is the 1920 Haiyuan earthquake; in fact, this is the largest and most recent event (Ran *et al.*, 1997; Zhang *et al.*, 2005; Liu-Zeng *et al.*, 2007; Li *et al.*, 2014; Ren *et al.*, 2016). Based on geological mapping (Deng *et al.*, 1989), the surface fault trace of the 1920 Haiyuan earthquake was investigated in detail. The Haiyuan fault is a left-lateral strike-slip fault and contains 11 discontinuous secondary faults that are separated by pull-apart basins with different sizes. Based on the geometry and geomorphology, the Haiyuan fault is divided into three segments (Zhang *et al.*, 2005). The western segment is approximately 100 km long, with a N60°W average strike. The middle segment is approximately 70 km long, with a N55°W strike. The eastern segment of the Haiyuan fault is approximately 80 km long and has a greater thrust component. The strike of the segment is N35°W, differing by approximately 20° from the overall strike of the Haiyuan fault. Depths of small earthquakes have been 3–25 km in these segments since 1976, as shown in Figure 1c. Liu *et al.* (2013) revealed an approximately 128 km fault trace with unprecedented clarity, using the airborne light detection and ranging

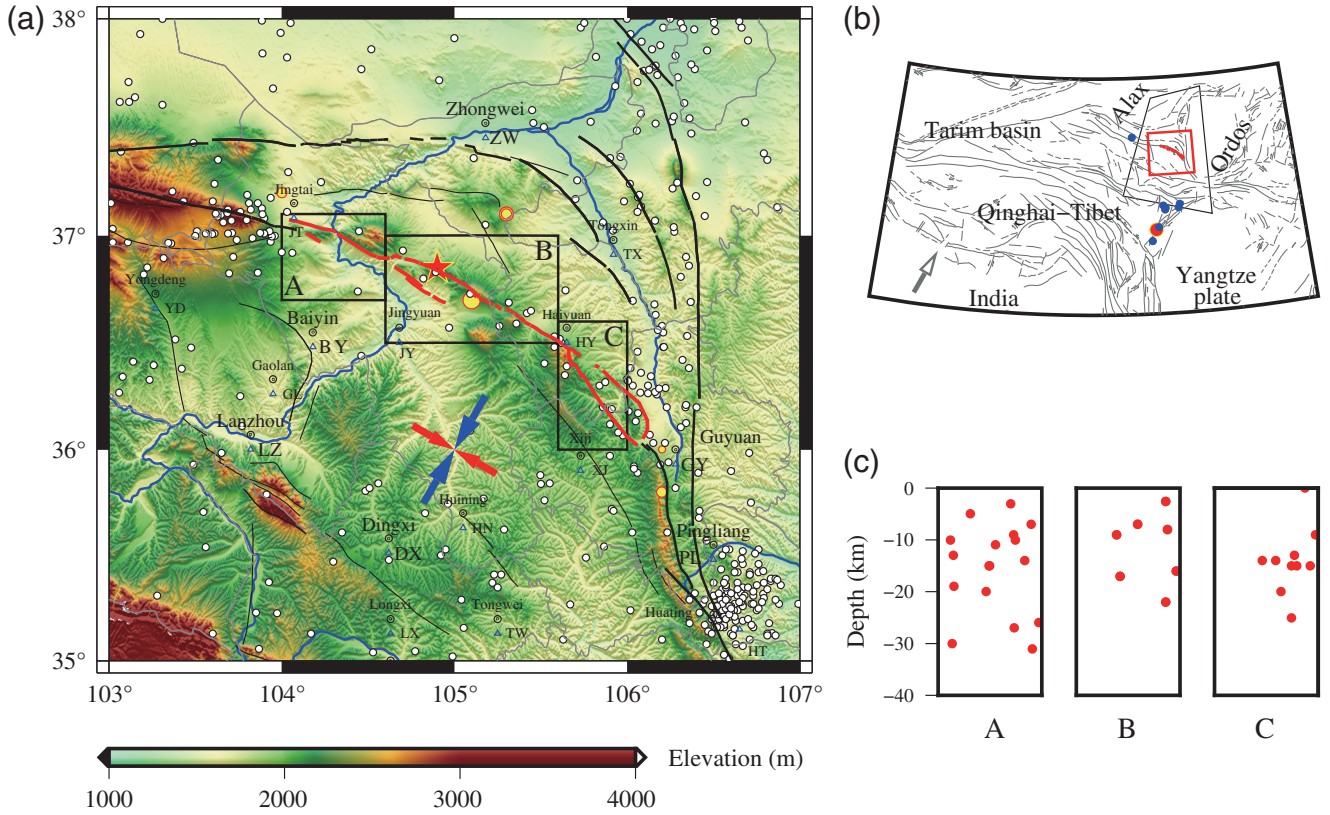

Figure 1. (a) Fault distribution in the study area. The red line is the surface rupture of the 1920 Haiyuan earthquake. The gray line represents the administrative region. Blue lines represent the rivers in the region. The yellow circles represent aftershocks of the 1920 Haiyuan earthquake above M_w 5. The red star represents the source hypocenter. The arrows represent the direction of horizontal principal stress. A, western segment; B, middle segment; and C, eastern segment. The blue triangles represent the assumed stations. The black circles filled with white represent earthquakes that took place after 1969. (b) Tectonic area surrounding the study area, which is the junction of the Alxa block, Ordos block, and Qinghai–Tibet block. The blue circles indicate earthquakes above M_w 6 after the 1976 Tangshan earthquake near the study area, and the red circle marks the 2008 M_w 7.9 Wenchuan earthquake. The gray arrow shows the north–east convergence direction of the Indian plate. The black box represents the north segment of the south–north belt. (c) Depths of small earthquakes near three segments A, B, and C of the Haiyuan fault after 1976 (China Seismic Catalog).

method. In addition, deep seismic reflection profiles (Li *et al.*, 2002; Fan *et al.*, 2004) revealed that the middle segment of the Haiyuan fault dips steeply from the surface ground to a depth of 10 km and is an ultracrustal fault (a deep fault cutting the Moho). Magnetotelluric sounding profiles (Zhan *et al.*, 2004) also reflected that the Haiyuan fault is an ultracrustal fault. However, based on high-resolution deep seismic reflection profiling, Wang *et al.* (2012) indicated that the western segment of the Haiyuan fault is not just a simple steep plane, but a fault with very complex geometry. Therefore, the geometry of the Haiyuan fault at depth is obscure to date.

The moment magnitude of the Haiyuan earthquake remains debatable. The M_s 8.5 value for the Haiyuan earthquake (Richter, 1958) has been widely accepted. Chen and Molnar (1977) estimated a moment magnitude of M_w 8.3, based on the hypothesis of a 45° dip angle using three seismograms. However, Abe (1981) argued that the older estimated magnitudes for the 1920 Haiyuan earthquake may have been overestimated. Then, Ou *et al.* (2018, 2019) re-estimated the magnitude of the 1920 Haiyuan earthquake, using a combined geological and seismic approach. Considering the horizontal offsets measured from orthorectified high-resolution Pleiades satellite imagery, the magnitude is $M_w = 7.64 \pm 0.12$. At the same time, digital historical seismograms were modeled to give body- and surface-wave magnitudes of $m_B = 7.89 \pm 0.29$ and $M_s = 8.22 \pm 0.21$, respectively. Therefore, considering the uncertainty, the moment magnitude of the 1920 Haiyuan earthquake was M_w 7.6 ~ 8.3. Moreover, the epicenter of the 1920 Haiyuan earthquake varies according to the different catalogs (Table 1). In addition, the maximum value of the horizontal dislocation on the ground surface is different in previous research results. The value of the maximum dislocation reaches 10–11 m based on geological mapping (Deng *et al.*, 1989). However, the value is approximately 7 m through the analysis of trenches (Ran *et al.*, 1997). In addition, Ren *et al.* (2016) inferred that the maximum displacement of 10–11 m was likely due to at least two earthquakes, and the maximum displacement from the studies of each one was ~5 m.

A dynamic rupture simulation may provide useful insights to constrain conditions of the 1920 Haiyuan earthquake. Previous studies tried to simulate the 1992 Landers earthquake (Olsen *et al.*, 1997; Peyrat *et al.*, 2001; Aochi and Fukuyama, 2002; Wollherr *et al.*, 2019), the 2008 Wenchuan earthquake (Duan, 2010; Wen *et al.*, 2012), the 2010 Haiti earthquake (Douilly *et al.*, 2015), and the 2015 Nepal earthquake (Wang *et al.*, 2017), based on dynamic rupture simulations. Their results provided reasonable models that would help evaluate strong ground motion and assess seismic hazards.

In this work, we found reasonable source models using 3D curved-grid finite-difference modeling to explain the observed information, including the dislocation inferred from the geological data. Based on the source models, we simulated the strong ground motion and analyzed the seismic disaster with seismograms and a theoretical intensity distribution.

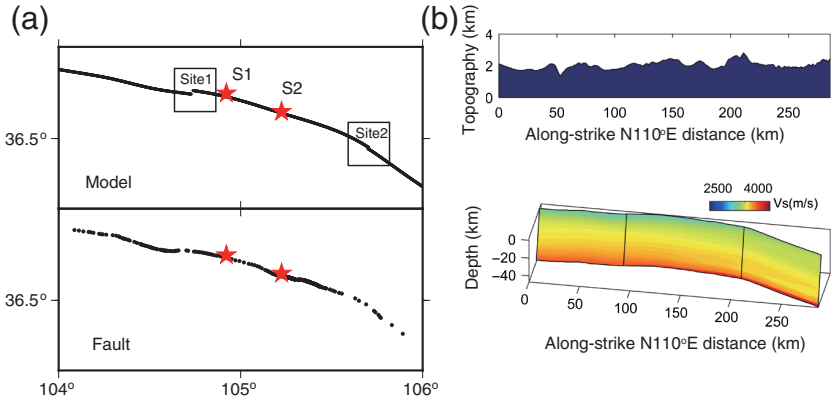

Figure 2. (a) Fault traces of the 1920 Haiyuan earthquake on the ground: (top panel) our simulation model and (bottom panel) observed data. The red stars represent the source hypocenter. The rectangles in the top panel outline the two sites with different jump distances. (b) The fault geometry in 3D space. The upper picture represents topographical variations along the fault-strike direction. The lower picture illustrates the velocity of the rocks around the fault plane.

Method and Fault Model

The numerical method used to simulate the dynamic rupture of the 1920 Haiyuan earthquake was proposed by Zhang *et al.* (2014a), based on the curved-grid finite-difference method (Zhang and Chen, 2006). The method uses the collocated grid for the finite-difference method, in which all physical values, such as the stress tensor, velocity, and Lame constants, are located at the same grid point. The governing equation for fault rupture propagation is a first-order velocity-stress formulation of the elastodynamic equations:

$$\rho v_{i,t} = \sigma_{ij,j}$$
$$\sigma_{ij,t} = \lambda v_{k,k}\delta_{ij} + \mu(v_{i,j} + v_{j,i}),$$

in which v_i is the ith component of particle velocity, σ_{ij} is the ijth component of the stress tensor, $\delta_{ij}$is the Kronecker delta, λ and μ are the Lame constants, and ρ is the density. To simulate the dynamic rupture and seismic-wave propagation with a topographic surface and a nonplanar fault, the governing equations are solved in curvilinear coordinates (Zhang *et al.*, 2014a). In addition, the split-nodes method (Day *et al.*, 2005) is adopted to better deal with discontinuous boundaries across the fault, and the slip-weakening law (Andrews, 1976a) is used to calculate the friction strength. In addition, the perfectly matched layer approach is carried out to absorb outgoing waves at truncated boundaries (Zhang *et al.*, 2014b). The advantages of this method include not only its computational efficiency and easy implementation, but also its flexibility in modeling ruptures with complex geometries. The accuracy and robustness of the method have been validated with benchmarks (Harris *et al.*, 2018) for rupture dynamic simulation. Moreover, the method has been applied to provide a scenario earthquake on the Jiaocheng fault in China (Zhang *et al.*, 2017).

Because the epicenter of the 1920 Haiyuan earthquake is different based on the various data sources (Table 1), two models with different hypocenters are considered in our simulation, as shown in Figure 2a. According to the catalog of historical felt earthquakes in China, the epicenter is located at S1 (104.9° E, 36.7° N). However, as determined by the Institute of Geology, China Earthquake Administration and the Seismological Bureau of Ningxia-Hui Autonomous Region (1990), the epicenter is located at S2 (105.3° E, 36.5° N). The Haiyuan fault geometry is constructed following the characteristics of three segments proposed by Zhang *et al.* (2005). However, the stepover widths around sites 1 and 2 are unclear. In this article, we set a 1.2 km stepover width around site 2, between the middle and eastern segments of the fault. At site 1, two different stepover widths of 1.8 and 2.5 km are considered, as shown in Table 2. Thus, for each epicenter position, three models are investigated: one continuous fault model and two discontinuous fault models with different stepover widths (Table 2). The surface topography (SRTM_PLUS15) is also considered, as shown in Figure 2b. The dip angle is 70° toward the southeast (SE),

Table 1
Data Source of the Epicenter

Data Source	Epicenter	
	Longitude	Latitude
Catalog of historical felt earthquakes in China	104°54′	36°42′
Institute of Geology, China Earthquake Administration (1990)	105°21′	36°38′
USGS	105.606°	36.888°

USGS, U.S. Geological Survey.

Table 2
Geometry of the Source Model

Model	Hypocenter Position	Step-Over Width at Site 1 (km)	Step-Over Width at Site 2 (km)	Dip Angle
S11	(104.9° E, 36.7° N)	0	0	70°
S12	(104.9° E, 36.7° N)	1.8	1.2	
S13	(104.9° E, 36.7° N)	2.5	1.2	
S21	(105.3° E, 36.5° N)	0	0	
S22	(105.3° E, 36.5° N)	1.8	1.2	
S23	(105.3° E, 36.5° N)	2.5	1.2	

which is the average angle based on geological mapping results (Deng *et al.*, 1989), and the depth of the hypocenter is 17 km. The fault in our models is 286 km long and 50 km wide. The y axis is oriented N110°E, along the opposite direction of the Haiyuan fault, and the x axis is perpendicular to the fault strike. The 3D velocity model used in our simulation was proposed by Shen *et al.* (2016), based on ambient noise. The mean and standard deviation of the velocity values at each location are on a $0.5° \times 0.5°$ grid from the surface to a depth of 150 km.

Although estimating the principal stresses along the Haiyuan fault directly is difficult, a good model of the stress distribution can be obtained by other methods. First, we determine the direction of triaxial principal stresses. In geology, the east–west-trending Haiyuan fault results from the India–Asia collision (Tapponnier and Molnar, 1977) and is compressed by the Alxa, Ordos, and Qinghai–Tibet blocks. For the fault zone, the direction of the principal stress has been inverted in many studies. Xie *et al.* (2000) calculated the tectonic stress at 46 sites using fault sliding information. In their study, the principal compressive stress direction was approximately east-northeast-trending, and the maximum principal stress axis was horizontal. Zhang *et al.* (2012) showed that the direction of fast shear waves corresponds with the strike of the Haiyuan fault, using the seismic anisotropy method in the crust. The fast shear waves are oriented nearly east–west and west-northwest at the Yongdeng and Jingtai stations, respectively. Yang *et al.* (2012) analyzed the characteristics of measured stress in the shallow Chinese mainland, using the database of crustal stress in China and adjacent area, the latest hydraulic fracturing data, and stress relief measurement data. They indicated that the principal stress increases with depth and that the maximum principal stress is horizontal within the depth of the study in the northern part of the north–south seismic belt. Sheng *et al.* (2015) determined the northeast principal stress directions via the inversion of focal mechanisms near the Haiyuan fault. Global Positioning System (GPS) data also showed that the strain rate changed from north–east to east–west along the Haiyuan fault (Liu *et al.*, 2007). We estimate the relative principal stress using the factor R as follows:

$$R = \frac{(\sigma_2 - \sigma_3)}{(\sigma_1 - \sigma_3)},$$

in which σ_1 is the maximum principal stress, σ_3 is the minimum principal stress, and σ_2 is the intermediate principal stress. For the strike-slip fault triaxial stress regime, the vertical stress is the intermediate principal stress ($\sigma_v = \sigma_2$). The maximum and minimum principal stress axes are horizontal (Célérier, 1988; Peng and Zhang, 2007; Célérier *et al.*, 2012). Thus, the factor R can be rewritten as

$$R = \frac{(\sigma_v - \sigma_h)}{(\sigma_H - \sigma_h)},$$

in which σ_H is the horizontal maximum principal stress and σ_h is the horizontal minimum principal stress. The factor R is 0.3–0.8, as inverted from the fault sliding information (Xie *et al.*, 2000). Wang *et al.* (2015) estimated the factor R as 0.66 by inverting the focal mechanisms. In addition, the effective normal stress increases with depth due to the fluid pressure in the crust. We define the pore-fluid factor for the level of fluid pressure changing with depth:

$$\lambda_v = \left(\frac{P_f}{\sigma_v'}\right) = \left(\frac{P_f}{\rho g h}\right),$$

in which ρ is the average rock density, g is the gravitation acceleration, and P_f is the fluid pressure. The effective vertical normal stresses (σ_v) for strike-slip faults are necessary to activate mesh structures (Sibson, 1996).

$$\sigma_v = (\sigma_v' - P_f) = (1 - \lambda_v)\rho g h, \qquad (0.4 < \lambda_v < 1.0).$$

In this article, we use the trial-and-error approach to find the optimum direction, by varying the orientation of the maximum principal stress direction (N0°E–N90°E). The directions of the maximum stress on the three segments are N45°E, N55°E, and N70°E, from west to east. At present, there is no information about tectonic stress before the 1920 Haiyuan earthquake. Thus, we can only obtain stress information after the 1920 Haiyuan earthquake. Because no earthquake has exceeded M_s 8.5 since the 1920 Haiyuan earthquake, and the last earthquake had occurred more than 1,000 years earlier, all events in the catalog that were used to do the stress orientation inversion happened in the stress field of ~100 years after the 1920 Haiyuan earthquake. We assume that the regional stress field is globally unchanged before and after the 1920 Haiyuan earthquake. We test six models with $R = 2/3$. In addition, the magnitudes of the triaxial stresses are calculated as follows:

$$\sigma_v = (1 - \lambda_v)\rho g h,$$
$$\sigma_H = 1.2\sigma_v,$$
$$\sigma_h = 0.6\sigma_v,$$

in which $\lambda_v = 0.95$. The initial stress on the fault is from the projection of triaxial stress ($R = 0.67$) with an irregular geometry (Fig. 3). The normal stress T_n increases with depth. The

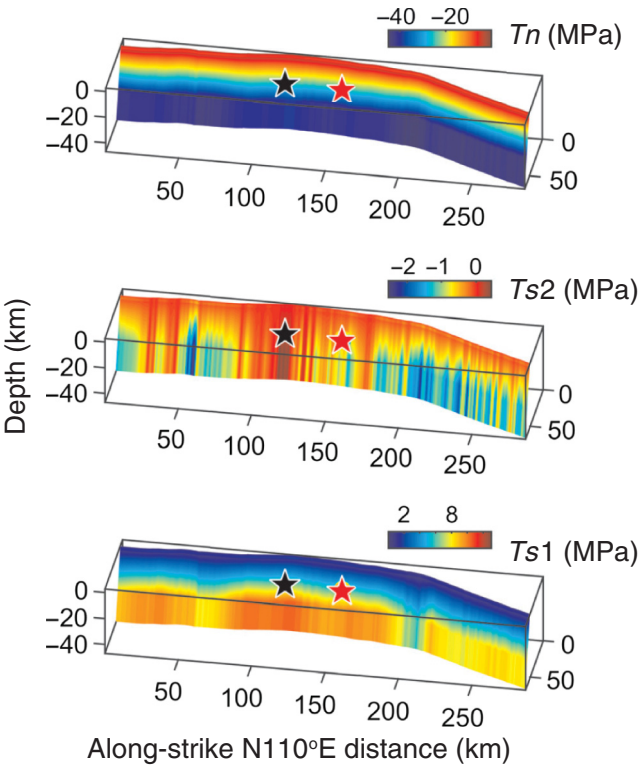

Figure 3. Initial stress distributions on the fault plane for different hypocenter locations. The stars represent epicenter S1 (black) and epicenter S2 (red). T_n represents the normal stress on the fault plane. T_{S1} and T_{S2} represent the shear stresses in the strike and dip directions, respectively.

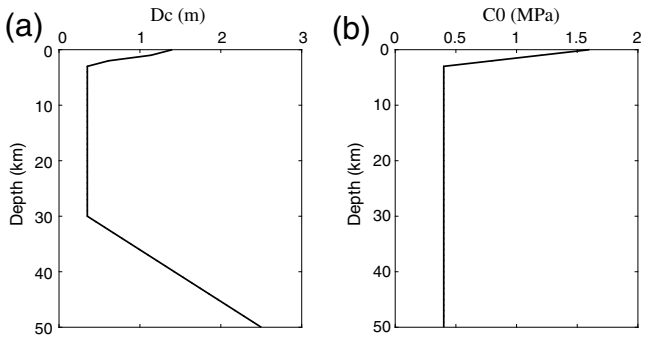

Figure 4. Schematics to illustrate the distribution of (a) critical distance (Dc) and (b) friction cohesion ($C0$) variations with depth.

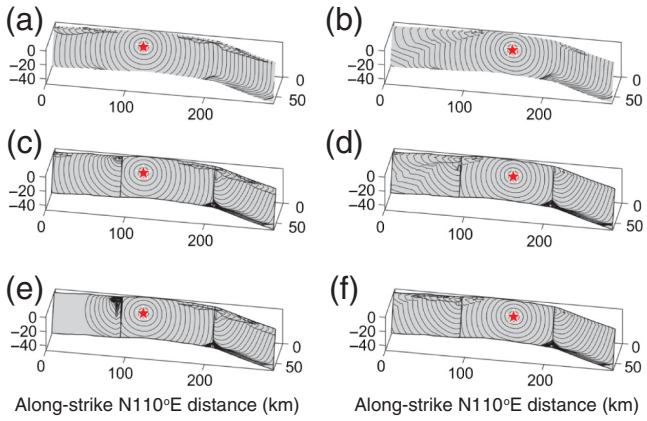

Figure 5. The contours of the rupture time at 2 s intervals for models (a) S11, (b) S21, (c) S12, (d) S22, (e) S13, and (f) S23. The red stars represent the locations of the hypocenters.

shear stress along the strike direction T_{S1} is heterogeneous, due to the irregular geometry. Positive values represent left-lateral slip. T_{S2}, which represents the shear stress in the dip direction, also changes with the geometry. $T_{S2} > 0$ represents normal slip, and vice versa. Moreover, the nucleation patches in the six models have the same size (with a radius of 5 km), hypocenter depth, and initial shear stress (0.1% higher than the strength).

Here, we consider the slip-weakening friction law (Ida, 1972; Andrews, 1976a,b) with a static friction coefficient (μ_s) of 0.4 and a dynamic friction coefficient (μ_d) of 0.1. The initial critical slip-weakening distance (Dc) and cohesion ($C0$) are depth dependent (Aochi *et al.*, 2003; Zhang *et al.*, 2017), as shown in Figure 4.

Results

Dynamic Rupture Simulation

The model space for the dynamic rupture is 60, 300, and 64 km in the x, y, and z coordinate directions, respectively. The model space for the ground-motion simulation is larger and is described in the Strong Ground Motion section. The computational space is divided into $300 \times 1500 \times 320$ grid points, with a grid spacing of 200 m and a timestep of 0.01 s. The total computed time window for the rupture propagation is 80 s. Figure 5 shows the rupture time contours for the six models, with a time interval of 2 s. Figures 6–8 illustrate snapshots of the slipping rate along the strike direction for different models. The final slip distributions on the fault plane for each model are shown in Figure 9. Figure 10 shows the dislocation distribution on the ground surface for each model.

From the dynamic rupture processes of the six models, we found that the rupture could not propagate to the entire fault in the time window of 80 s for model S13. Thus, we mainly analyze the results of the other five models and do not consider model S13 for the 1920 Haiyuan earthquake in this article.

For the continuous fault models S11 and S21, the rupture propagation is bilateral, as shown in Figure 5a,b. We find locally supershear rupture near the free surface for the two models. In addition, for model S21, the obvious supershear rupture appears on the ground surface at 25 s on the western segment of the fault (Fig. 6b), and then the supershear rupture propagates from the ground surface to depth. The patterns of the final slip distribution for the two models are different near the hypocenter and the principal direction of

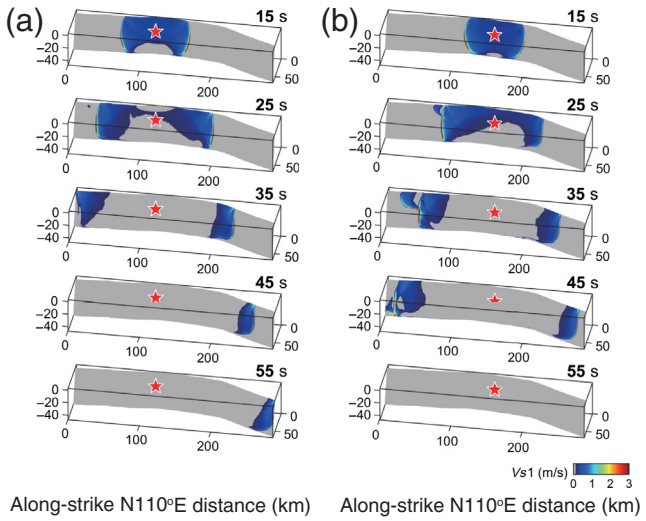

Figure 6. Snapshots of rupture propagation along the strike direction for models (a) S11 and (b) S21.

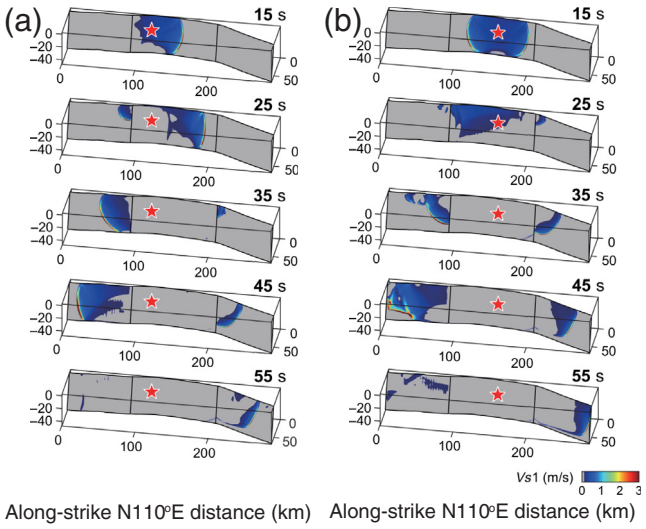

Figure 7. Snapshots of rupture propagation along the strike direction for models (a) S12 and (b) S22.

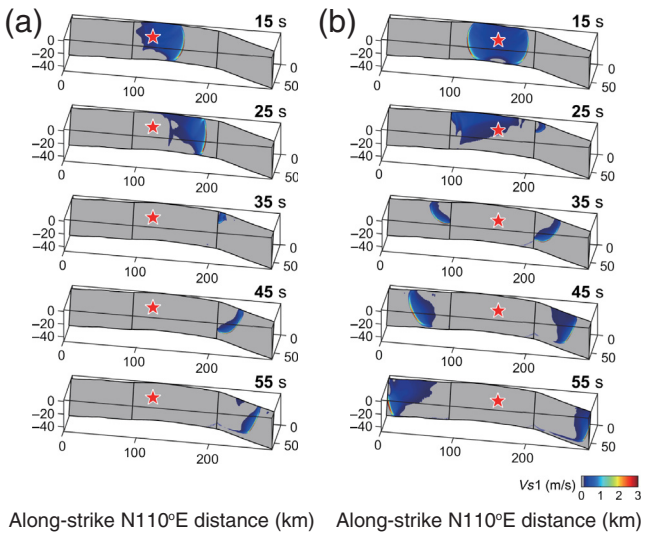

Figure 8. Snapshots of rupture propagation along the strike direction for models (a) S13 and (b) S23.

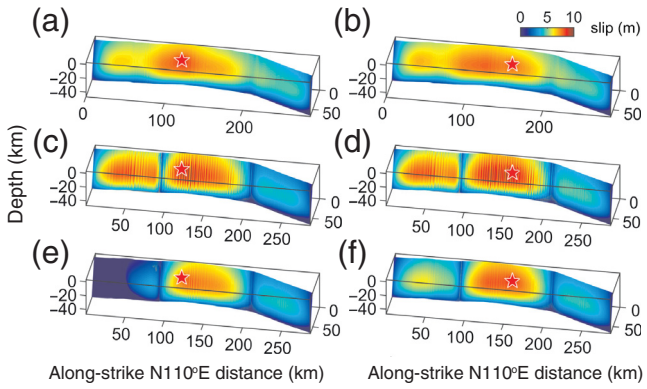

Figure 9. The distribution of the final slip for the six models (a) S11, (b) S21, (c) S12, (d) S22, (e) S13, and (f) S23. The red stars represent the locations of the hypocenters.

the rupture (Fig. 9a,b). In particular, the slip on the western segment for model S21 is larger than that for model S11 at the depth of the hypocenter. Then, we calculated the seismic moment M_0 and moment magnitude M_w for each model. The seismic moment is $M_0 = 2.34 \times 10^{21}$ N · m for S11 and $M_0 = 2.40 \times 10^{21}$ N · m for S21, according to the moment magnitudes of M_w 8.21 and 8.22, respectively.

For models S12 and S22, the fault plane is disconnected with a 1.8 km stepover width at site 1. The rupture propagates across the entire fault and lasts approximately 77 s. As shown in Figures 5c,d and 7, when the rupture jumps from the middle segment to the adjacent segments, the slip starts at the surface and propagates toward the down-dip direction. In addition, the stepover plays the role of a barrier as the rupture propagates. For example, the rupture propagates to the western segment a certain distance for model S11, while the rupture just jumps to the western segment for model S12 at 25 s. For model S21, the supershear rupture obviously occurs at 25 s, whereas the supershear rupture obviously appears at 35 s for model S22. However, the final slip distribution is similar for the two models on the two ends of the fault with similar initial rupture points on the free surface (Fig. 9c,d). The seismic moment is $M_0 = 2.35 \times 10^{21}$ N · m for S12 and $M_0 = 2.43 \times 10^{21}$ N · m for S22, corresponding to the moment magnitudes of M_w 8.21 and 8.22, respectively.

For models S13 and S23, the stepover width at site 1 (2.5 km) is larger than that for models S12 and S22 (1.8 km). Hu *et al.* (2016) indicated that the jump distance decreases as the accelerating length of the rupture front on the main fault before rupture jump (ALRF: the accelerating length of the

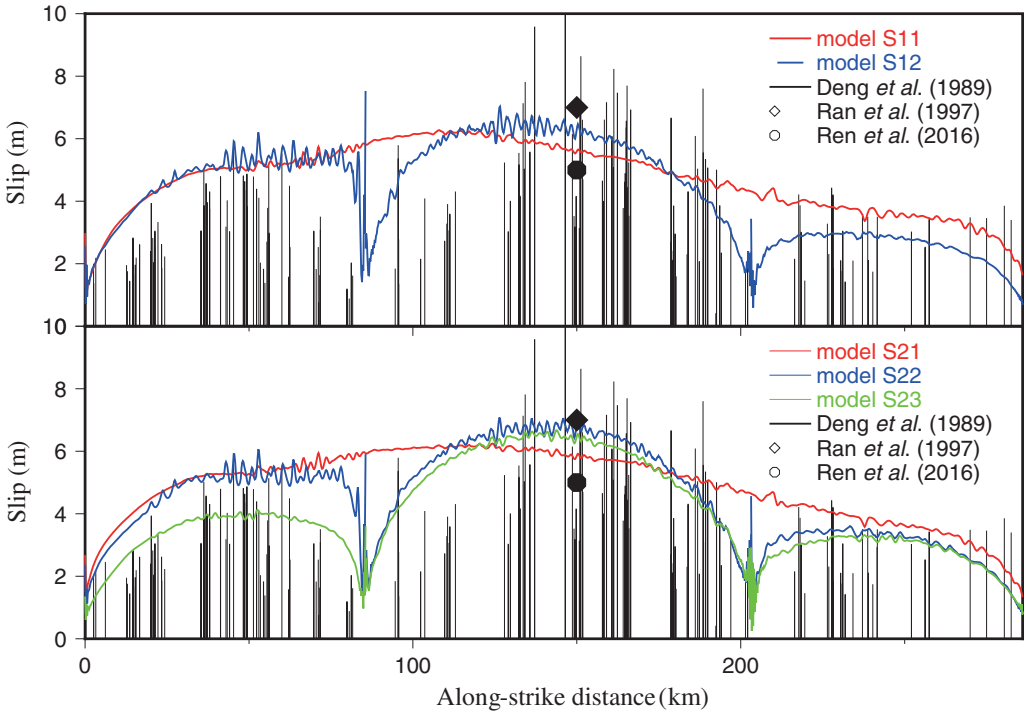

Figure 10. The calculated horizontal displacement for each model and the observations.

rupture front on the main fault before rupture jump) decreases. Thus, the rupture can easily propagate to the western segment for model S23 with a larger ALRF, whereas the rupture jumps to the western segment for model S13 after 55 s. The supershear rupture also appears at the free surface when the rupture propagates to the western segment, as shown in Figure 8. The characteristics of the final slip distribution for model S23 are similar to those for model S22. However, the values of the slip for model S23 (~4 m) are smaller than those for model S22 (~5.5 m) on the western segment of the fault. For S23, $M_0 = 2.14 \times 10^{21}$ N · m and M_w 8.19.

Because only the surface displacement information for the 1920 Haiyuan earthquake is available, we extract the surface displacement of the five models for comparison. Based on geologic mapping at the 1:50,000 scale (Deng *et al.*, 1989), the distribution of surface displacement obeys an approximately Gaussian distribution across the entire fault and along each segment. The displacement on the western segment of the fault (~6 m) is larger than that on the eastern segment of the fault (~4 m). We find that the surface displacement distributions of models S12 and S22 fit the observations better, as shown in Figure 10. In addition, the rupture features for these models are consistent with the multiple rupture characteristics of the 1920 Haiyuan earthquake discussed by Huan *et al.* (1991). Because the epicenters have little effect on the surface displacement, we cannot confine the source point of the 1920 Haiyuan earthquake from the simulation of the rupture process. Therefore, we simulated strong ground motion associated with the 1920 Haiyuan earthquake to constrain the epicenter.

Strong Ground Motion

Based on the simulation of dynamic rupture results for models S12 and S22, we simulated strong ground motion. The computational space is 330 km in the latitudinal direction, 440 km in the longitudinal direction, and 60 km in the depth direction, with a grid spacing of 500 m and a timestep of 0.018 s. The total computed time window for seismic-wave propagation is 200 s. The method and velocity model are discussed in the previous sections of this article. Because of the directivity effect, the ground motion in front of the rupture propagation is larger than that in the opposite direction, which can be found from the seismograms and the intensities of the two models. On the premise that there are stations, located in the cities shown in Figure 1a, we obtained the seismograms shown in Figure 11. For source model S12 with the principal rupture direction to the SE, the horizontal component of particle velocity at the HY station, located ~90 km from the epicenter, is the largest among these stations. For source model S22 with the principal rupture direction of northwest, the horizontal component of the particle velocity at the JT station, located ~130 km from the epicenter, is the largest among these stations. In addition, we derive the horizontal peak ground velocity (PGVh) distribution in the study area. Then, we analyze the theoretical hazard distribution given the relationship between PGVh and intensity, which is based on the Chinese seismic intensity scale, as shown in Figure 12. Figure 12a,b shows the distribution of PGVh and intensity for model S12. The maximum PGVh occurs near Haiyuan County, where the intensity reaches XI. For model S22, the

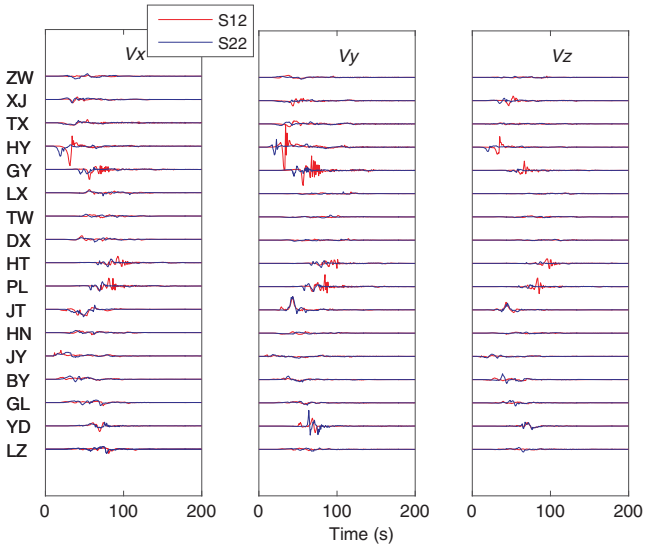

Figure 11. Seismograms showing the velocities for 17 sites in the study area for models S12 and S22.

maximum PGVh and high-intensity values occur near Jingtai County. In addition, the horizontal components of the particle velocity (V_x: east–west component and V_y: south–north component) throughout are larger than the vertical component (V_z), which is consistent with the maximum horizontal stress regime of the model.

The characteristics of theoretical intensity distribution, based on model S12, better conform to field investigations by Gu (1989) (Fig. 13). Thus, source model S12 is more reasonable for the 1920 Haiyuan earthquake. However, the intensity values are notably smaller than the actual intensity values in most regions, as shown in Table 3. One reason may be that we adopt a velocity model without considering the site conditions. In the study region, Tertiary and Quaternary sediments are widely distributed. In addition, shallow sediments can enhance the peak ground velocity up to twice its value (Hough *et al.*, 1990; Ding *et al.*, 2004; Qin *et al.*, 2012). Another reason may be that the frequency of the seismic waves in our model is relatively low (~0.4 Hz). In our simulation of strong ground motion, the grid spacing is 500 m and the maximum frequency is ~0.4 Hz. High-frequency seismic waves have great influence on the intensity (Wald *et al.*, 1999), which is not considered in our model. Thus, the intensity estimated in most of the study area is lower than the values estimated during the investigation.

Discussion

The Maximum Slip on the Ground Surface

Synthesizing the previous simulations, we prefer model S12 to simulate the dynamic rupture and strong ground motion for the 1920 Haiyuan earthquake. However, the maximum slip on the ground surface (~6.5 m), based on model S12, is smaller than that from geological investigations (~10 m) (Gu, 1989). One reason for this discrepancy may be the result of the locally high-stress drop, similar to the simulation of the 2008 Wenchuan earthquake by Wen *et al.* (2012). Another reason, as mentioned in the Introduction, is that the observed displacement is cumulative and includes those from the 1920 Haiyuan earthquake and aftershocks with a maximum magnitude of ~7. The latter reason has recently gained popularity (Ran *et al.*, 1997; Ren *et al.*, 2016). Thus, we consider an aftershock of ~M_w 7 that ruptured to the ground surface. In Figure 1c, the seismic activity is strong at a depth of 20 km. The fault plane is 70 × 25 km, and the hypocenter is located at S2 with a 15 km depth. The cohesion $C0$ decreases from 0.4 to 0.2 MPa. The initial rupture time contours and final distribution are shown in Figure 14. The seismic moment is $M_0 = 6.14 \times 10^{19}$ N · m, according to a moment magnitude of M_w 7.16. The maximum slip on the fault plane is ~2.5 m, and the displacement on the ground surface is ~1 m. Therefore, we infer that the displacement for the 1920 Haiyuan earthquake, as determined during the field investigation, is probably the cumulative slip.

The Influence of Variations in Dip Angle with Depth

As previously mentioned, the fault plane of S12 is composed of three disconnected faults, with a 70°dip angle inferred from the field investigation. Considering the complex deep structure, Duan *et al.* (2018) estimated the detailed dip angle for the Haiyuan fault, based on seismic data. They indicated that the dip angle is approximately 80°, at a depth of 8 km on the whole fault. For the western segment, the dip angle changes to a vertical angle, except for a small change at 9 km. For the middle and eastern segments, the dip angle decreases with depth, including some abrupt changes. Considering the simple grid setup, we set the dip angle to gradually change along the strike and dip directions of the fault, as shown in Figure 15. We find that a small dip angle plays the role of a barrier in slowing the rupture propagation. The rupture front is obviously slower at depth on the eastern segment (Fig. 16). Therefore, the variations in dip angle with depth have a significant influence on rupture propagation and require further investigation in future work.

Implications of Modeling Results for Fault Systems

In our simulation, the 1920 Haiyuan earthquake includes multiple subevents on the Haiyuan fault. This phenomenon is common in large strike-slip earthquakes (Wesnousky, 2006; Xu *et al.*, 2002, 2006). Stress accumulation on the main fault over a period of time may break through the yield strength on a secondary fault at a specific distance. In this article, the stepover is 1.8 km, and the dynamic rupture can easily jump to the adjacent segment. It is more difficult for a rupture to jump a wider stepover. The stepover is 4 km on the western end of the Haiyuan fault segment, where the distance is too large for the rupture to jump across the subfaults. In addition, the slip deficit at the junction of the secondary fault may reflect the disconnected subfaults. On the basic premise of elastic rebound theory (Reid, 1910), rupture would occur until elastic strains

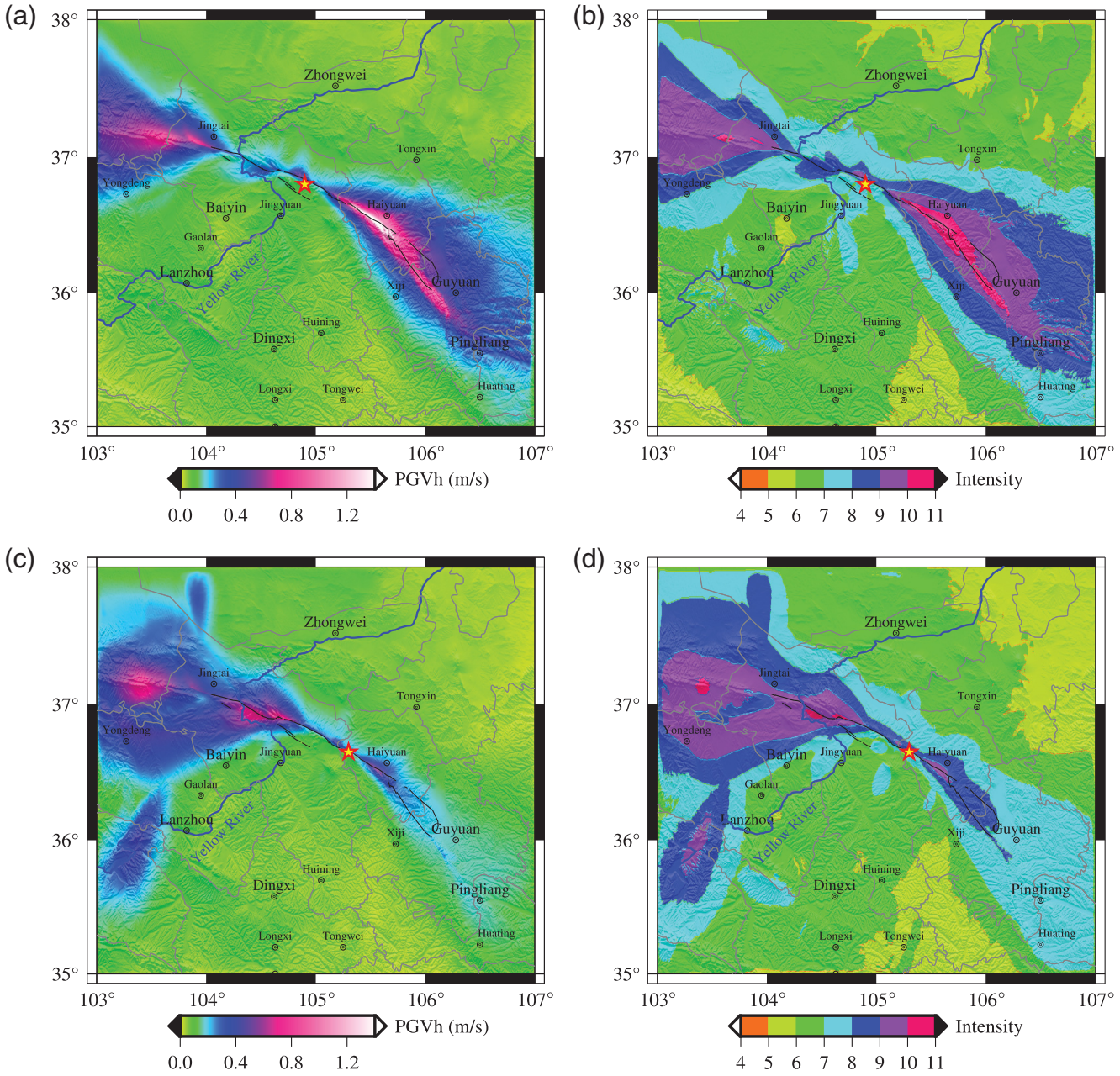

Figure 12. The distribution of horizontal peak ground velocity (PGVh) and the intensity map for the earthquakes triggered at different locations. (a) The PGVh distribution for model S12, (b) the intensity distribution for model S12, (c) the PGVh distribution for model S22, and (d) the intensity distribution for model S22. The red stars represent the locations of the hypocenters. The black lines represent the surface rupture of the 1920 Haiyuan earthquake.

become high enough, usually along an existing fault zone, and slippage would rebound to a less deformed state. Then, the accumulation of elastic deformation and the release of energy in a sudden rebound would be repeated. The 1920 Haiyuan earthquake was a large intraplate earthquake, and such earthquakes occur infrequently. From the paleoearthquake events, the recurrence interval of earthquakes is approximately 1000 years, and the rupture patterns of earthquakes are different (Ren *et al.*, 2016). Therefore, we infer that the 1920 Haiyuan earthquake and aftershocks released the fracture energy and that the seismic activity is weak (Fig. 1a). Moreover, the seismic activity is higher, and stress accumulates more easily at the ends of the Haiyuan fault, especially on the western Haiyuan fault, based on the inversion of Interferometric Synthetic Aperture Radar data and GPS data (Cui *et al.*, 2009; Jolivet *et al.*, 2012).

Conclusions

Based on the dynamic rupture simulations, we found the best-fitting dynamic source model for the 1920 M_s 8.5

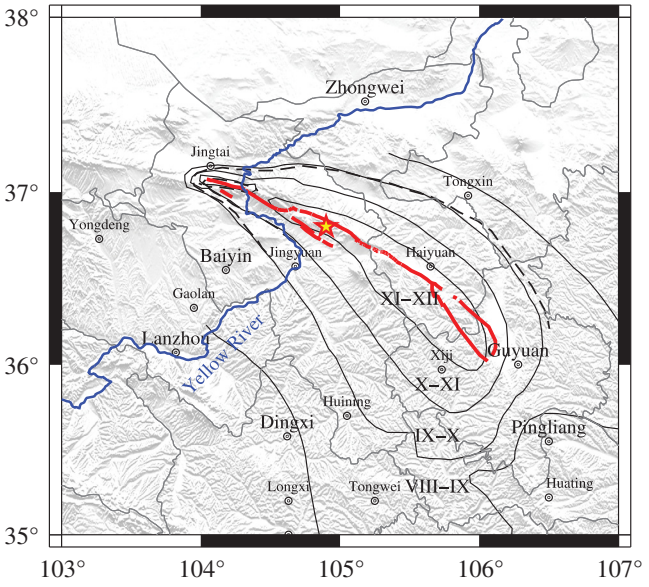

Figure 13. Contour lines representing the intensities from the investigation by Gu (1989). The red lines represent the surface rupture of the 1920 Haiyuan earthquake. The red stars represent the locations of the hypocenters.

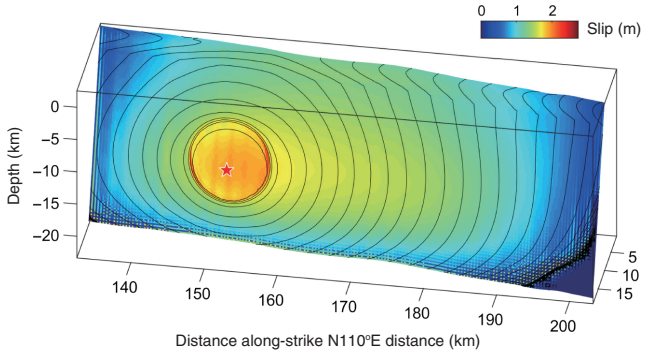

Figure 14. Initial rupture time with 1 s interval and the final slip distribution on the fault plane for the aftershock with $M_w \sim 7$.

Table 3
Intensity Values in Some Regions

Regions	Theoretical Intensity Values	Intensity Based on Models
Haiyuan County	X–XI	XI–XII
Jingtai County	VIII–IX	XI–XII
Xiji County	VIII–IX	X–XI
Guyuan County	IX–X	IX–X
Baiyin city	V–VI	VIII–IX
Jingyuan County	VII–VIII	IX–X
Tongxin County	VI–VII	VIII–IX

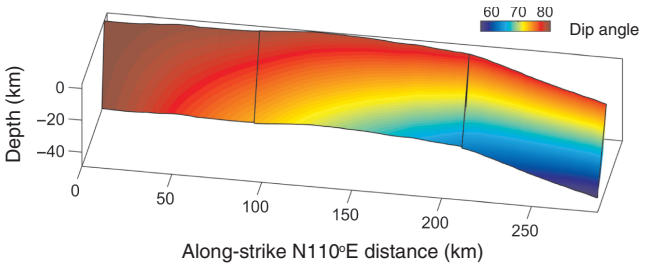

Figure 15. Dip angle distribution on the fault plane (modified from Duan *et al.*, 2018).

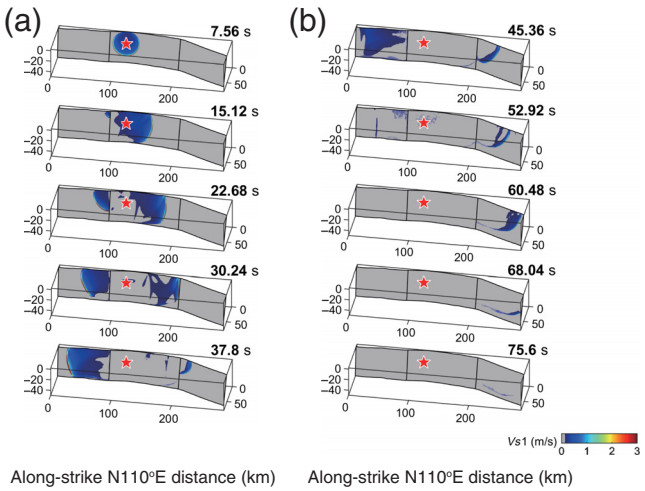

Figure 16. Snapshots of rupture propagation along the strike direction for the model with changing dip angle.

Haiyuan earthquake. Five models with different hypocenters and fault geometries are discussed. Our models show that the epicenter not only influences the dynamic rupture process, but also affects the final slip distribution (S12 and S22). We find that the rupture speed is faster when the epicenter is located far from the western segment (S12 and S22). Interestingly, the displacements on the ground surface for the models with the same geometry are similar. The final distributions for S12 and S22 fit with the observations, but they show different PGVh distributions and intensities (Fig. 12). In addition, the geometry of the fault has great influence on the final slip distribution. The rupture front gradually propagates from the nucleation zone to both ends of a fault with a continuous fault plane. The final slip distribution on the ground surface smoothly decreases from the epicenter toward the ends. Nevertheless, the displacement distribution on the ground surface for a fault with a disconnected fault plane has its own Gaussian distribution. For the subfaults, the larger the jump distance is, the smaller the displacement.

The dynamic rupture simulation of the 1920 Haiyuan earthquake shows that a simple fault, dipping at 70° and composed of three disconnected subfault planes, can match the

observations well. Besides, the epicenter (104.9° E, 36.7° N) and maximum slip (~6.5 m) on the ground surface are reasonable for this earthquake. The displacement distribution and intensity simulated here agree well with those from the field investigations. In addition, the dynamic rupture process has shown that the 1920 Haiyuan earthquake was caused by multiple subevents.

Data and Resources

The elevation data are from ftp://topex.ucsd.edu/pub/srtm15_plus/topo15.grd (last accessed August 2018) and the 3D velocity model is from http://ciei.colorado.edu/Models/ (last accessed February 2019).

Acknowledgments

The comments from Ying Chang, Associate Editor Delphine D. Fitzenz, Peter Moczo, and other anonymous reviewers are much appreciated. This work is supported by the National Key R&D Program of China (2017YFC1500205) and by the National Natural Science Foundation of China (Grant Numbers 41790465, 41774044).

References

Abe, K. (1981). Magnitudes of large shallow earthquakes from 1904 to 1980, *Phys. Earth Planet. In.* **27,** 72–92.

Andrews, D. J. (1976a). Rupture propagation with finite stress in antiplane strain, *J. Geophys. Res.* **81,** 3575–3582.

Andrews, D. J. (1976b). Rupture velocity of plane strain shear cracks, *J. Geophys. Res.* **81,** 5679–5687.

Aochi, H., and E. Fukuyama (2002). Three-dimensional nonplanar simulation of the 1992 Landers earthquake, *J. Geophys. Res.* **107,** ESE 4-1–ESE 4–12.

Aochi, H., R. Madariaga, and E. Fukuyama (2003). Constraint of fault parameters inferred from nonplanar fault modeling, *Geochem. Geophys. Geosys.* **4,** no. 2, 1020, doi: 10.1029/2001GC000207.

Célérier, B. (1988). How much does slip on a reactivated fault plane constrain the stress tensor?, *Tectonics* **7,** 1257–1278.

Célérier, B., A. Etchecopar, F. Bergerat, P. Vergely, F. Arthaud, and P. Laurent (2012). Inferring stress from faulting: From early concepts to inverse methods, *Tectonophysics* **581,** 206–219.

Chen, W.-P., and P. Molnar (1977). Seismic moments of major earthquakes and the average rate of slip in central Asia, *J. Geophys. Res.* **82,** 2945–2969.

Cui, D. X., Q. L. Wang, Y. X. Hu, and G. Z. Zhu (2009). Inversion of GPS data for slip rates and locking depths of the Haiyuan fault, *Acta Seismol. Sinica* **31,** 516–525.

Day, S. M., L. A. Dalguer, N. Lapusta, and Y. Liu (2005). Comparison of finite difference and boundary integral solutions to three-dimensional spontaneous rupture, *J. Geophys. Res.* **110,** no. B12307, doi: 10.1029/2005JB003813.

Deng, Q., W. Zhang, P. Zhang, D. Jiao, F. Song, Y. Wang, B. C. Burchfiel, P. Molnar, L. Royden, and S. Chen (1989). Haiyuan strike-slip fault zone and its compressional structures of the end, *Seismol. Geol.* **11,** 1–14.

Ding, Z., Y. T. Chen, and G. F. Panza (2004). Estimation of site effects in Beijing City, *Pure Appl. Geophys.* **161,** 1107–1123.

Douilly, R., H. Aochi, E. Calais, and A. M. Freed (2015). Three-dimensional dynamic rupture simulations across interacting faults: The Mw 7.0, 2010, Haiti earthquake, *J. Geophys. Res.* **120,** 1108–1128.

Duan, B. (2010). Role of initial stress rotations in rupture dynamics and ground motion: A case study with implications for the Wenchuan earthquake, *J. Geophys. Res.* **115,** no. B05301, doi: 10.1029/2009JB006750.

Duan, H., S. Zhou, and R. Li (2018). Estimation of dip angle of Haiyuan faults based on seismic data, *Chin. J. Geophys.* **61,** 3713–3721 (in Chinese).

Fan, J., S. Li, X. Zhang, and M. Liu (2004). Geometric form of Haiyuan fault zone in the crustal interior and dynamics implications, *Acta Seismol. Sinica* **17,** 43–51.

Gu, G. (1989). *Catalogue of Chinese Earthquakes:(1831 BC-1969 AD)*, CRC Press, Beijing, China.

Harris, R. A., M. Barall, B. Aagaard, S. Ma, D. Roten, K. Olsen, B. Duan, D. Liu, B. Luo, and K. Bai (2018). A suite of exercises for verifying dynamic earthquake rupture codes, *Seismol. Res. Lett.* **89,** 1146–1162.

Hough, S. E., P. A. Friberg, R. Busby, E. F. Field, K. H. Jacob, and R. D. Borcherdt (1990). Sediment-induced amplification and the collapse of the Nimitz Freeway, *Nature* **344,** 853–855.

Hu, F., Z. Zhang, and X. Chen (2016). Investigation of earthquake jump distance for strike-slip step overs based on 3-D dynamic rupture simulations in an elastic half-space, *J. Geophys. Res.* **121,** 994–1006.

Huan, W., M. Gu, and X. Chang (1991). Multiple rupture characteristics of the 1920 Haiyuan M8. 5 earthquakes, *Acta Seismol. Sinica* **13,** 21–30.

Ida, Y. (1972). Cohesive force across the tip of a longitudinal-shear crack and Griffith's specific surface energy, *J. Geophys. Res.* **77,** 3796–3805.

Institute of Geology, China Earthquake Administration and the Seismological Bureau of Ningxia-Hui Autonomous Region (1990). *The Haiyuan Active Fault Zone*, Seismology Publishing House, Beijing, China (in Chinese).

Jolivet, R., C. Lasserre, M.-P. Doin, S. Guillaso, G. Peltzer, R. Dailu, J. Sun, Z.-K. Shen, and X. Xu (2012). Shallow creep on the Haiyuan fault (Gansu, China) revealed by SAR interferometry, *J. Geophys. Res.* **117,** no. B06401, doi: 10.1029/2011JB008732.

Lanzhou Institute of Seismology and the Seismological Bureau of Ningxia-Hui Autonomous Region (1980). *The Haiyuan Earthquake in 1920*, Seismology Publishing House, Beijing, China (in Chinese).

Li, S.-L., X.-K. Zhang, C. Zhang, J. Zhao, and S. Cheng (2002). A preliminary study on the crustal velocity structure of Maqin-Lanzhou-Jingbian by means of deep seismic sounding profile, *Chin. J. Geophys.* **45,** 210–217.

Li, Y., Y. Ran, H. Wang, and F. Wu (2014). Paleoseismic records of large earthquakes on the cross-basin fault in the Ganyanchi pull-apart basin, Haiyuan fault, northeastern Tibetan Plateau, *Nat. Hazards* **71,** 1695.

Liu, J., T. Chen, P. Zhang, H. Zhang, W. Zheng, Z. Ren, S. Liang, C. Sheng, and W. Gan (2013). Illuminating the active Haiyuan fault, China by airborne light detection and ranging, *Chin. Sci. Bull.* **58,** 41–45.

Liu, M., Y. Yang, Z. Shen, S. Wang, M. Wang, and Y. Wan (2007). Active tectonics and intracontinental earthquakes in China: The kinematics and geodynamics, *Geol. Soc. Am. Spec. Pap.* **425,** 299–318.

Liu-Zeng, J., Y. Klinger, X. Xu, C. Lasserre, G. Chen, W. Chen, P. Tapponnier, and B. Zhang (2007). Millennial recurrence of large earthquakes on the Haiyuan fault near Songshan, Gansu Province, China, *Bull. Seismol. Soc. Am.* **97,** 14–34.

Olsen, K. B., R. Madariaga, and R. J. Archuleta (1997). Three-dimensional dynamic simulation of the 1992 Landers earthquake, *Science* **278,** 834–838.

Ou, Q., G. Kulikova, J. Yu, A. J. Elliott, R. T. Walker, and B. Parsons (2019). Combining geological and seismological methods to re-estimate the magnitude of the 1920 Haiyuan earthquake, *SSA Technical Sessions*, The Westin Seattle, Washington, 23–26 April 2019.

Ou, Q., J. Yu, G. Kulikova, B. Parsons, and R. T. Walker (2018). Magnitude of the 1920 Haiyuan (China) earthquake re-estimated using a combined geological and seismological approach, *AGU Fall Meeting Abstracts*, Washington, D.C., 10–14 December 2018.

Peng, S., and J. Zhang (2007). *Engineering Geology for Underground Rocks*, Springer Science & Business Media, Berlin-Heidelberg, Germany.

Peyrat, S., K. Olsen, and R. Madariaga (2001). Dynamic modeling of the 1992 Landers earthquake, *J. Geophys. Res.* **106,** 26,467–26,482.

Qin, Y., Y. Wang, H. Takenaka, and X. Zhang (2012). Seismic ground motion amplification in a 3D sedimentary basin: The effect of the vertical velocity gradient, *J. Geophys. Eng.* **9,** 761–772.

Ran, Y., R. Duan, Q. Deng, D. Jiao, and W. Min (1997). 3-D trench excavation and paleoseismology at Gaowanzi of the Haiyuan fault, *Seismol. Geol.* **19,** 97–107.

Reid, H. F. (1910). *The Mechanics of the Earthquake*, Carnegie Institution of Washington, Washington, D.C.

Ren, Z., Z. Zhang, T. Chen, S. Yan, J. Yin, P. Zhang, W. Zheng, H. Zhang, and C. Li (2016). Clustering of offsets on the Haiyuan fault and their relationship to paleoearthquakes, *Geol. Soc. Am. Bull.* **128,** 3–18.

Richter, C. F. (1958). *Elementary Seismology*, WH Freeman and Company, San Francisco, California, 136–139.

Shen, W., M. H. Ritzwoller, D. Kang, Y. Kim, F.-C. Lin, J. Ning, W. Wang, Y. Zheng, and L. Zhou (2016). A seismic reference model for the crust and uppermost mantle beneath China from surface wave dispersion, *Geophys. J. Int.* **206,** 954–979.

Sheng, S.-Z., Y. Wan, J.-C. Huang, Y.-F. Bu, and L. Xiang (2015). Present tectonic stress field in the Circum-Ordos region deduced from composite focal mechanism method, *Chin. J. Geophys.* **58,** 436–452 (in Chinese).

Shi, W., Y. Liu, Y. Liu, P. Chen, L. Chen, M. Cen, X. F. Huang, and H. Q. Li (2013). Cenozoic evolution of the Haiyuan fault zone in the northeast margin of the Tibetan Plateau, *Earth Sci. Front.* **20,** 1–17.

Sibson, R. H. (1996). Structural permeability of fluid-driven fault-fracture meshes, *J. Struct. Geol.* **18,** 1031–1042.

Tapponnier, P., and P. Molnar (1977). Active faulting and tectonics in China, *J. Geophys. Res.* **82,** 2905–2930.

Wald, D. J., V. Quitoriano, T. H. Heaton, and H. Kanamori (1999). Relationships between peak ground acceleration, peak ground velocity, and modified Mercalli intensity in California, *Earthq. Spectra* **15,** 557–564.

Wang, H.-Y., R. Gao, A. Yin, X.-S. Xiong, C.-Y. Kuang, W.-H. Li, and W.-Y. Huang (2012). Deep structure geometry features of Haiyuan Fault and deformation of the crust revealed by deep seismic reflection profiling, *Chin. J. Geophys.* **55,** 3902–3909.

Wang, X.-S., J. Lu, Z.-J. Xie, F. Long, X.-Y. Zhao, and Y. Zheng (2015). Focal mechanisms and tectonic stress field in the north-south seismic belt of China, *Chin. J. Geophys.* **58,** 4149–4162 (in Chinese).

Wang, Y., S. M. Day, and M. Denolle (2017). Dynamic rupture models of the 2015 M_W 7. 8 Nepal earthquake, *AGU Fall Meeting Abstracts*, New Orleans, Louisiana, 11–15 December 2017.

Wen, Y.-Y., D. D. Oglesby, B. Duan, and K.-F. Ma (2012). Dynamic rupture simulation of the 2008 Mw 7.9 Wenchuan earthquake with heterogeneous initial stress, *Bull. Seismol. Soc. Am.* **102,** 1892–1898.

Wesnousky, S. G. (2006). Predicting the endpoints of earthquake ruptures, *Nature* **444,** no. 7117, 358–360.

Wollherr, S., A.-A. Gabriel, and P. M. Mai (2019). Landers 1992 "reloaded": Integrative dynamic earthquake rupture modeling, *J. Geophys. Res.* **124,** 6666–6702, doi: 10.1029/2018JB016355.

Xie, F., S. Shu, S. Dou, S. Zhang, and X. Cui (2000). Quaternary tectonic stress field in the region of Haiyuan-Liupanshan fault zone to Yinchuan fault-depression, *Seismol. Geol.* **22,** 139–146.

Xu, X., W. Chen, W. Ma, G. Yu, and G. Chen (2002). Surface rupture of the Kunlunshan earthquake (Ms 8.1), northern Tibetan plateau, China, *Seismol. Res. Lett.* **73,** 884–892.

Xu, X., G. Yu, Y. Klinger, P. Tapponnier, and J. Van Der Woerd (2006). Reevaluation of surface rupture parameters and faulting segmentation of the 2001 Kunlunshan earthquake (Mw7. 8), northern Tibetan Plateau, China, *J. Geophys. Res.* **111,** no. B05316, doi: 10.1029/2004JB003488.

Yang, S.-X., R. Yao, X.-F. Cui, Q.-C. Chen, and L.-Y. Huang (2012). Analysis of the characteristics of measured stress in Chinese mainland and its active blocks and north-south seismic belt, *Chin. J. Geophys.* **55,** 4207–4217.

Zhan, Y., G. Z. Zhao, X. B. Chen, J. Tang, J. J. Wang, and Q. H. Deng (2004). Crustal structure from magnetotelluric profiling in the Haiyuan earthquake area, Ningxia Hui Autonomous Region, China, *Chin. J. Geophys.* **47,** 274–281.

Zhang, W., and X. Chen (2006). Traction image method for irregular free surface boundaries in finite difference seismic wave simulation, *Geophys. J. Int.* **167,** 337–353.

Zhang, H., Y. Gao, Y.-T. Shi, X.-F. Liu, and Y.-X. Wang (2012). Tectonic stress analysis based on the crustal seismic anisotropy in the northeastern margin of Tibetan plateau, *Chin. J. Geophys.* **55,** 95–104.

Zhang, P., W. Min, Q. Deng, and F. Mao (2005). Paleoearthquake rupture behavior and recurrence of great earthquakes along the Haiyuan fault, northwestern China, *Sci. China Earth Sci.* **48,** 364–375.

Zhang, Z., W. Zhang, and X. Chen (2014a). Three-dimensional curved grid finite-difference modelling for non-planar rupture dynamics, *Geophys. J. Int.* **199,** 860–879.

Zhang, Z., W. Zhang, and X. Chen (2014b). Complex frequency-shifted multi-axial perfectly matched layer for elastic wave modelling on curvilinear grids, *Geophys. J. Int.* **198,** 140–153.

Zhang, Z., W. Zhang, X. Chen, and C. Fu (2017). Rupture dynamics and ground motion from potential earthquakes around Taiyuan, China, *Bull. Seismol. Soc. Am.* **107,** 1201–1212.

Xiurong Xu
Feng Hu
School of Earth and Space Sciences
University of Science and Technology of China
No. 96, JinZhai Road, Baohe District
Hefei, Anhui 230026, China
xuxr@mail.ustc.edu.cn
hufeng07@ustc.edu.cn

Zhenguo Zhang
Xiaofei Chen
Department of Earth and Space Sciences
Southern University of Science and Technology
1088 Xueyuan Avenue
Shenzhen, Guangdong 518055, China
zhangzg@sustech.edu.cn
chenxf@sustech.edu.cn

Manuscript received 8 March 2019;
Published Online 10 September 2019